Analysis of State-Specific Vibrations Coupled to the Unidirectional Energy Transfer in Conjugated Dendrimers

Miguel A. Soler,[†] Adrian E. Roitberg,[§] Tammie Nelson,[‡] Sergei Tretiak,[‡] and Sebastian Fernandez-Alberti*,[†]

[†]Universidad Nacional de Quilmes, Roque Saenz Peña 352, B1876BXD Bernal, Argentina

[‡]Theoretical Division, Center for Nonlinear Studies (CNLS), and Center for Integrated Nanotechnologies (CINT), Los Alamos National Laboratory, Los Alamos, New Mexico 87545, United States

[§]Quantum Theory Project, Department of Chemistry, University of Florida, Gainesville, Florida 32611, United States

ABSTRACT: The nonadiabatic excited-state molecular dynamics (NA-ESMD) method and excited-state instantaneous normal modes (ES-INMs) analyses have been applied to describe the state-specific vibrations that participate in the unidirectional energy transfer between the coupled chromophores in a branched dendrimeric molecule. Our molecule is composed of two-, three-, and four-ring linear poly(phenyleneethynylene) (PPE) units linked through meta-substitutions. After an initial laser excitation, an ultrafast sequential $S_3 \rightarrow S_2 \rightarrow S_1$ electronic energy transfer from the shortest to longest segment takes place. During each $S_n \rightarrow S_{n-1}$ (n = 3, 2) transition, ES-INM(S_n) and ES-INM(S_{n-1}) analyses have been performed on S_n and S_{n-1} states, respectively. Our results reveal a unique vibrational mode localized on the S_n state that significantly matches with the corresponding nonadiabatic coupling vector $\mathbf{d}_{n,(n-1)}$. This mode also corresponds to the highest frequency ES-INM(S_n) and it is seen mainly during the electronic transitions. Furthermore, its absence as a unique ES-INM(S_{n-1}) reveals that state-specific vibrations play the main role in the efficiency of the unidirectional $S_n \rightarrow S_{n-1}$ electronic and vibrational energy funneling in light-harvesting dendrimers.
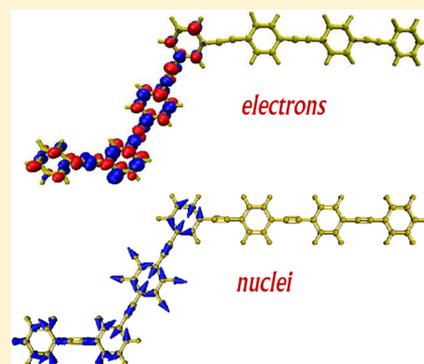
I. INTRODUCTION

Dendrimers are highly branched conjugated macromolecules that act as efficient light-absorbing antennas. Their structures mimic those found in nature possessing numerous peripheral groups with branched repeat units and a core, similar to a tree. These unique architectures create highly efficient energy funnels; energy absorbed at the periphery undergoes ultrafast unidirectional transport through the dendritic branches toward the core. High precision in the topology, flexibility, and solubility properties of dendrimers can be achieved due to advances in their controlled synthesis.[1−6] The detailed understanding of the electronic and vibrational energy funneling throughout dendritic macromolecules constitutes a major challenge for their potential applications as scaffolds for light-harvesting devices.

Among the large variety of dendritic macromolecules, those composed of poly(phenyleneethynylene) (PPE) units have received special theoretical and experimental interest due to their highly efficient unidirectional energy-transfer properties.[7−13] These properties have been extensively probed by Moore et al.[7,8,14,15] on the perylene-terminated dendrimer called the nanostar. The branched repeat units of the nanostar are built from linear PPE segments of different lengths linked by meta-substitutions at the branching phenylene nodes. The length of branched nodes decrease from the periphery to the core (four-, three-, and two-ring linear PPE units) creating an intramolecular energy gradient. When the peripheral two-ring

chromophores are initially excited, the energy is transferred nonradiatively down the branches to the core with nearly 100% efficiency.[8−12] The meta-branching localizes excitons within each linear PPE fragment hindering any further delocalization of electrons across the dendrimer framework.[8,16] Experimental evidence for this excitonic localization is observed by steady-state spectroscopy.[8] Therefore, the dendrimer molecule can be effectively represented as an ensemble of weakly coupled linear PPE chromophore units. Furthermore, the excitons in the nanostar are localized on each PPE unit, and its absorption spectrum can be predicted from the sum of the individual chromophore spectra.[7,10,14,17]

The fluorescence quantum yield of the nanostar, measured from steady-state and time-resolved fluorescence studies, reaches values near unity.[10,14] Therefore, ground-state recovery through an intramolecular nonradiative process is negligible. The fluorescence from the perylene chromophore (with fluorescence lifetime ∼2.3 ns) of the dendrimer undoubtedly indicates that intramolecular nonradiative singlet−singlet energy-transfer processes are involved. The ultrafast energy transfer inside PPE dendrimers has been experimentally shown at the time resolution of picoseconds[10] and femtoseconds,[18−20] revealing a stepwise energy transfer from the shorter

chromophore PE units to the longer PE chains. These experiments indicate that intermediate steps in the energy transfer take place on a subpicosecond time scale. Furthermore, the existence of different pathways for the energy migration makes these macromolecules a compelling target for quantum control schemes.[20]

To simulate a dendrimer's excited-state structure and optical properties, such as absorption spectra, the Frenkel exciton Hamiltonian model[21-24] has been successfully applied, revealing a complex interplay of electronic couplings across the molecular network.[25,26] Furthermore, the dendrimer molecule can be understood as an ensemble of linear chromophore units with a weak charge transfer between them. As a result, the excitons in the nanostar are localized on each PPE segment[8] and its overall absorption spectrum can be interpreted as the sum of these individual contributions.[10,14] Atomistic calculations of the ultrafast electronic and vibrational energy transfer in a dendritic molecule, however, requires the simulation of the dynamics of the polyatomic molecule on the multidimensional potential energy landscape involving several coupled electronic excited states. In our previous work, we have developed a nonadiabatic excited-state molecular dynamics (NA-ESMD)[27] framework suitable for dealing with photo-induced dynamics in large molecular systems consisting of hundreds of atoms on time scales of tens of picoseconds. The method uses actual excited-state potential energy surfaces, gradients, and nonadiabatic couplings calculated accounting for many-body effects in the excited state (i.e., configuration interaction singles (CIS) or time-dependent Hartree–Fock (TDHF) approximation). This method has been successfully applied to demonstrate the highly efficient ultrafast energy transfer between the linear PPE building blocks of the nanostar.[73,74] Simulations at low temperature have revealed that the system undergoes strong coupling between electronic excited states in a sequential order, and the couplings involve only one pair of states at a time. An intramolecular vibrational energy redistribution, in which the ethynylene C–C triple bonds play a critical role, has been shown to be concomitant with the electronic energy transfer.

In this work, we explore the role of molecular vibrations on electronic energy transfer between the individual coupled chromophore units in a branched dendritic molecule. The model molecular system is composed of two-, three-, and four-ring linear poly(phenyleneethynylene) (PPE) units linked through meta-substitutions. Our aim is to identify the nature of the state-specific vibrations related to electronic coupling and intramolecular energy transfer. Vibrational motions of polyatomic molecules can be elucidated using equilibrium normal modes (ENM) analysis.[28-31] The ENMs are computed from the diagonalization of the mass-weighted Hessian matrix at the local minimum of the potential. Therefore, the application of this methodology to study nonequilibrium dynamics of photoinduced processes presenting ultrafast energy transfer among several coupled electronic states may not be appropriate. Vibrational anharmonicities and couplings eventually make it quite difficult to keep the identity of each individual ENM. An alternative way to undertake this problem is to use instantaneous normal modes (INMs),[32-34] which are obtained by diagonalizing the mass-weighted Hessian matrix at each instantaneous configuration (geometry) of the molecule. After introduction of adequate coordinate displacements, the INMs provide an instantaneous decoupled description of the

vibrational motions of the molecule at the corresponding time-dependent configuration.[35]

Though the INMs were originally developed to study short-time dynamics properties of liquids,[36-41] this concept has been widely extended to deal with vibrational dynamics of polyatomic molecules.[42-45] Consequently, we use the NA-ESMD framework in combination with ES-INM analyses performed on each individual electronic excited state involved in the process.

One advantage of analyzing the nuclear motion in terms of the INMs coordinates is that the leading short time contributions to the evolution of the potential energy can be described as the sum of individual decoupled contributions.[32] At any instantaneous molecular geometry, the configurational space can be divided into orthogonal (INM) directions.[46] The complexity of the potential energy surface of the molecule introduces anharmonicities that induce coupling between the INMs. This leads to a limitation in the validity of the INMs to the vicinity of the configuration from which they have been obtained. Consequently, the INMs should not be interpreted as real harmonic nuclear motions but as instant vibrational coordinates through which the nonequilibrium molecular dynamics can be analyzed. Previous theoretical and experimental studies validate the use of INMs to analyze non-equilibrium vibrational relaxation processes.[42,47-50] In this paper, we consider the INMs as a basis set of dynamical variables that can be used to describe the nuclear motion to help us understand the photoinduced dynamics. The INMs conveniently represent the complex potential energy hyper-surfaces of the molecule in terms of effective reaction coordinates characterizing nuclear motions involved in the photoinduced intramolecular energy-transfer process.

The paper is organized as follows. In section II we briefly review the NA-ESMD method and ES-INM analysis. In section III we present and discuss our computational results on the electronic and vibrational features examined particularly in regions of strong nonadiabatic couplings, revealing the chemical principles for the efficient funneling through the model dendritic molecule. Conclusions are given in section IV.

II. METHODS

A. NA-ESMD Framework. Our NA-ESMD approach[27,51,52] has been developed to simulate photoinduced dynamics in organic conjugated molecules involving multiple coupled electronic excited states. The code is particularly optimized to study intramolecular energy-transfer processes in large polyatomic conjugated molecules. The method uses *direct*[53] or *on the fly* analytical calculations of CIS energies,[54-56] gradients[27,57,58] and nonadiabatic couplings,[27,59-61] as calculated with the collective electron oscillator (CEO) method,[54,26,62,63] coupled to semiempirical Hamiltonian (here we use the AM1[64] model). The NA-ESMD method achieves a good compromise between accuracy and computational efficiency. A detailed discussion about the NA-ESMD implementation, advantages, and testing parameters can be found elsewhere.[27,68]

The molecular dynamics with quantum transitions[65-67] (MDQT) method developed by Tully et al. is implemented in NA-ESMD to provide an efficient description of the nonadiabatic dynamics reflected in the time evolution of the populations of the different electronic excited states involved in the process. Within our theoretical MDQT framework, we consider the simultaneous propagation of an electronic wave

function quantum mechanically while the nuclei move classically on a potential energy surface, which is defined by a single AM1/CIS electronic state at a given time. The time dependent electronic wave function $\psi(\mathbf{r},\mathbf{R},t)$ is expanded in the basis of adiabatic CIS basis functions $\phi_\alpha(\mathbf{r};\mathbf{R}(t))$ as

$$\psi(\mathbf{r},\mathbf{R},t) = \sum_\alpha c_\alpha(t)\,\phi_\alpha(\mathbf{r};\mathbf{R}(t)) \tag{1}$$

where $c_\alpha(t)$ are the time-dependent CIS expansion coefficients and $\mathbf{r}$ and $\mathbf{R}$ are the electronic and nuclear coordinates, respectively. Substitution of eq 1 into the time-dependent Schrödinger equation yields

$$i\hbar\frac{\partial c_\alpha(t)}{\partial t} = c_\alpha(t)E_\alpha - i\hbar\sum_{\beta\neq\alpha} c_\beta(t)\dot{\mathbf{R}}(t)\cdot\mathbf{d}_{\alpha\beta} \tag{2}$$

where E_α is the αth eigenvalue of the CIS matrix calculated at time t, $\dot{\mathbf{R}} = \partial R/\partial t$ are nuclear velocities, and $\mathbf{d}_{\alpha\beta} = \langle\phi_\alpha(\mathbf{r};\mathbf{R}(t))|\nabla_{\mathbf{R}}\phi_\beta(\mathbf{r};\mathbf{R}(t))\rangle$ is the nonadiabatic coupling vector. The integration of eq 2 along the trajectory computes the amplitude of each quantum mechanical state as a function of time. The relative changes of the $c_\alpha(t)$ coefficients dictate transitions from one electronic surface to another for the classical nuclear motion. These values are governed by the strength of time-dependent nonadiabatic couplings $\dot{\mathbf{R}}\cdot\mathbf{d}_{\alpha\beta}$. The probabilities of hopping from one state to another are dictated by the value of the nonadiabatic couplings, in accordance with the MDQT approach.

Within the MDQT approach, a large number of independent trajectories is required to achieve the desired convergence of the results. In a recent article[68] we have analyzed in detail the impact that the number of trajectories and various other parameters have on the simulations.

At this point, it is important to discuss the convenience of our NA-ESMD implementation to deal with state-specific vibrations that lead to electronic couplings. At nuclear configurations where the time evolution of the electronic wave function $\psi(\mathbf{r},\mathbf{R},t)$ is dominated by one particular electronic state $\phi_\alpha(\mathbf{r};\mathbf{R}(t))$ without interacting with the other states ($\dot{\mathbf{R}}\cdot\mathbf{d}_{\alpha\beta}\approx 0$), the nuclear dynamics is dictated solely by the forces on that state. The amplitude of more than one state becomes relevant when departure from adiabaticity takes place, and distinct possible paths for the nuclear dynamics emerge. For cases in which the classical dynamics depends strongly on the quantum path, an average mixing treatment of the nuclear forces will not reproduce the true dynamics correctly. Surface hopping methods, like MDQT, have been developed to deal with these branching processes.[69−71] Within these methods, the wave function responsible for determining the forces on the classical particles is never a mixed state, and trajectories always evolve on a single potential electronic energy surface at a given time. Therefore, good classical/quantum motion correlation is retained. With this aspect in mind, it becomes crucial to identify the role that nuclear differential motions on the different excited-state potential energy surfaces can have on photo-induced processes.

B. Excited-State Instantaneous Normal Modes (ES-INM) Analysis. The INM approach describes the intra-molecular vibrations at a given time as a set of well-defined and independent harmonic oscillators.[32−34] Within our NA-ESMD framework, the INM analysis is performed as follows. A set of mass-weighted Cartesian *space-fixed* coordinates, corresponding to the configuration $\mathbf{R}_0$ of the molecule at a given time t_0, is

translated and rotated to a *body-fixed* reference frame with the origin at the center of mass and axes corresponding to the principal axes of inertia. Within this Cartesian frame, the potential energy E_α for the N nuclei moving classically on the single α- electronic state is expanded up to second order as

$$E_\alpha(\mathbf{R}_0) = E_\alpha(\mathbf{R}_0) - \sum_{i=1}^{3N} F_\alpha^i(\mathbf{R}_0)\Delta\mathbf{R}_t^i$$
$$+ \frac{1}{2}\sum_{i=1}^{3N}\sum_{j=1}^{3N} H_\alpha^{ij}(\mathbf{R}_0)\Delta\mathbf{R}_t^i\Delta\mathbf{R}_t^j \tag{3}$$

where $\Delta\mathbf{R}_t^i \equiv \mathbf{R}_t^i - \mathbf{R}_0^i$ is the displacement of the atom $i = 1, ..., N$ with Cartesian coordinates $R^i \equiv (X^i, Y^i, Z^i)$. The coefficients of the linear and quadratic terms are the elements of the force $3N$ vector $\mathbf{F}_\alpha$ and the $(3N \times 3N)$ mass-weighted Hessian matrix $\mathbf{H}_\alpha$, both evaluated on the αth electronic state

$$F_\alpha^i(\mathbf{R}_0) = -\partial E_\alpha/\partial R^i|_{\mathbf{R}_0} \tag{4}$$

$$H_\alpha^{ij}(\mathbf{R}_0) = -\partial^2 E_\alpha/\partial R^i\partial R^j|_{\mathbf{R}_0} \tag{5}$$

The gradients (forces) are calculated analytically in the NA-ESMD,[27] whereas the second derivatives (the Hessian matrix) are computed numerically from finite differences of the gradients. Upon diagonalization of $\mathbf{H}_\alpha$, the set of ES-INM(S_α) vectors $\{\mathbf{Q}_\alpha^i\}_{i=1,3N}$ are defined by the corresponding eigenvector matrix $\mathbf{L}_\alpha$, which allows them to be expressed as a linear combination of Cartesian displacements,

$$\mathbf{Q}_\alpha^i(t) = \sum_{j=1}^{3N} l_\alpha^{ji}\Delta\mathbf{R}_t^j \tag{6}$$

Because the eigenvectors described in $\mathbf{L}_\alpha$ are orthogonal, we can also express the Cartesian displacements $\Delta\mathbf{R}^j(t)$ in terms of the INMs,

$$\Delta\mathbf{R}_t^j = \sum_{i=1}^{3N} l_\alpha^{ji}\mathbf{Q}_\alpha^i(t) \tag{7}$$

By substitution of this expression into eq 3, we can write the potential energy E_α in terms of the INMs as

$$E_\alpha(\mathbf{R}_0) = E_\alpha^0(\mathbf{R}_0) + \frac{1}{2}\sum_{i=1}^{3N} \lambda_\alpha^i(\mathbf{Q}_\alpha^i(t) + a_\alpha^i)^2 \tag{8}$$

where λ_α^i ($i = 1, ..., 3N$) are the eigenvalues of $\mathbf{H}_\alpha$ related to the vibrational frequencies $\nu_\alpha^i = (\lambda_\alpha^i)^{1/2}/2\pi$, and a_α^i are the coordinate shifts that account for the force term in eq 3 and are given by

$$a_\alpha^i = -\frac{1}{\lambda_\alpha^i}\sum_{j=1}^{3N} F_\alpha^j(\mathbf{R}_0)l_\alpha^{ji} \tag{9}$$

and $E_\alpha^0(\mathbf{R}_0)$ is the shift-corrected equilibrium potential,

$$E_\alpha^0(\mathbf{R}_0) = E_\alpha(\mathbf{R}_0) - \frac{1}{2}\sum_{i=1}^{3N} \lambda_\alpha^i(a_\alpha^i)^2 \tag{10}$$

In this way, the potential energy E_α at the instantaneous configuration $\mathbf{R}_0$ of the molecule can be decoupled in terms of the shifted normal coordinates $\mathbf{Q}_\alpha^i(t) + a_\alpha^i$. It is important to stress that the introduction of these displacements on the normal coordinates do not affect their momenta. Therefore, both sets of modes provide equivalent kinetic energy values. In

the present work, we do not attempt to express the potential energy in terms of the individual normal mode contributions. Instead we aim to analyze the instant decoupled directions provided by the set of ES-INM(S_α) vectors $\{\mathbf{Q}_\alpha^i\}_{i=1,3N}$. Because these directions are independent of the displacements, our discussion is presented in term of the original $\{\mathbf{Q}_\alpha^i\}_{i=1,3N}$.

C. Molecular Dynamics Simulations. The model molecule studied in this work is shown in Figure 1a. It is
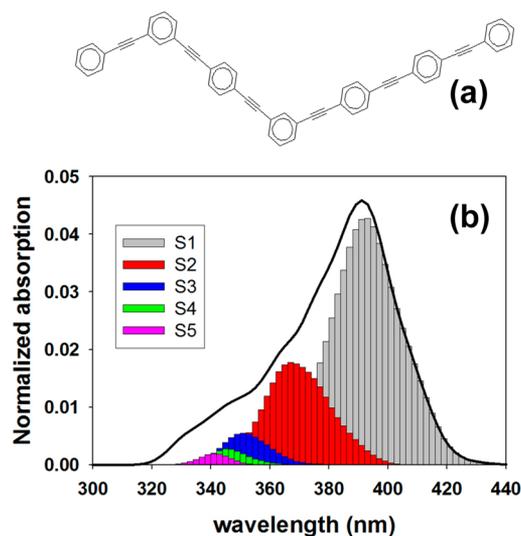
Figure 1. (a) Model dendritic molecule studied in this work involves two-, three-, and four-ring linear poly(phenyleneethynylene) units linked by meta-substitution. (b) Simulated absorption spectrum at 300 K (solid line) including contributions of all excited states considered in our NA-ESMD simulations.

composed of two-, three-, and four-ring linear poly-(phenyleneethynylene) (PPE) units linked through meta-positions, representing the branching phenylene building blocks of the nanostar.

The initial nuclei positions and momenta for the NA-ESMD simulations were taken from a ground-state AM1 equilibrated MD trajectory run at 300 K for 500 ps and using a classical time step $\Delta t = 0.5$ fs. Instead of choosing a predefined initial excited state for the excitation, we employ a method to mimic a Gaussian laser pulse. The initial excited state was chosen according to a Franck−Condon window defined as

$$g_\alpha(\mathbf{r},\mathbf{R}) = \exp[-T^2(E_{laser}(fs^{-1}) - \Omega_\alpha)^2] \quad (11)$$

where E_{laser} is the energy of a laser centered at 348 nm corresponding to the high-frequency peak in the theoretical absorption spectrum (Figure 1b) resulting from contributions of states S_n ($n \geq 3$). The laser line shape is assumed to be a Gaussian $f(t) = \exp(-t^2/2T^2)$, $T^2 = 42.5$ fs, which corresponds to a Gaussian fwhm (full width at half-maximum) = 100 fs. Thus, the initial excited state is selected according to the relative values of the $g_\alpha(\mathbf{r},\mathbf{R})$ weighted by the oscillator strengths of each state α.

For all simulations, the Langevin equation at constant room temperature,[72] with a friction coefficient $\gamma = 2.0$ ps^{-1}, was used.[72,73] The 10 lowest-energy AM1/CIS excited states and their corresponding time-dependent nonadiabatic couplings were included in the simulations. This level of theory has been previously validated for PPE dendrimers by comparison with time-dependent density functional theory (TDDFT) and

experimental results.[73,74] Four hundred NA-ESMD trajectories were propagated for 150 fs at 300 K. The nuclei are propagated with the velocity Verlet integration method[75] with a classical time step $\Delta t = 0.1$ fs, and the quantum amplitudes (eq 2) are propagated with a time step $\delta t = \Delta t/4$ using the code designed by Hull, Enright, and Jackson[76,77] that uses the Runge−Kutta−Verner fifth- and sixth-order method. Details on the NA-ESMD implementation and simulations can be found elsewhere.[27,68]

III. RESULTS AND DISCUSSION

The absorption spectrum of the branched dendritic molecule in Figure 1a was calculated using an equilibrated ground-state conformational sampling at 300 K, and it is shown in Figure 1b. The contributions of the different excited states are depicted by different colors. In agreement with our previous simulations done at 10 K,[73] the analysis of the state transition densities indicates that S_1 is localized mainly on the four-unit linear segment, whereas S_2 is localized mainly on the three-ring unit. Our previous results at 10 K have shown that S_4 was a state with high oscillator strength localized on the two-ring unit, whereas S_3 was an optically forbidden state localized on the four-ring unit. Nevertheless, our present results reveal that thermal perturbations at 300 K can interchange the energy ordering of these states. Therefore, the state that absorbs at 348 nm and having transition density localized on the two-ring unit can be attributed to either S_3 or S_4 depending on the molecule conformation at the moment of the laser excitation. As was pointed out previously,[73] these states undergo trivial unavoided crossings in the beginning of dynamics. As a result, S_3 remains localized on the two-ring unit and almost no $S_4 \rightarrow S_2$ transitions are observed in our simulations.

Figure 2 shows the time-dependence of the populations on each electronic excited state after photoexcitation, averaged
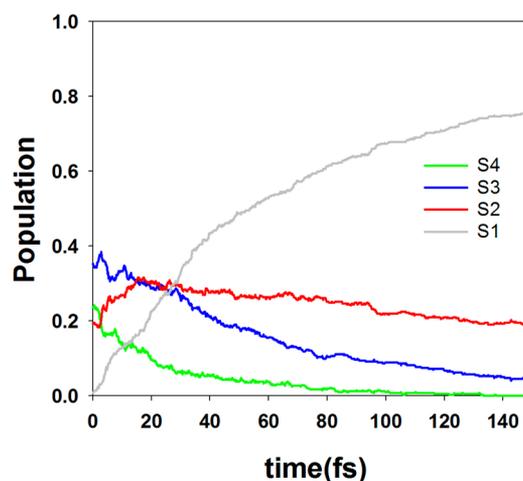
Figure 2. Population on each electronic state as a function of time obtained from the fraction of trajectories in each state.

over 400 trajectories. For the sake of simplicity, only the four lowest excited states are shown. As has been pointed out in section II.C, the probability for starting from a given electronic state is obtained according to the relative values of the $g_\alpha(\mathbf{r},\mathbf{R})$ weighted by the oscillator strengths of each state α. The resulting final ratio was 19% (S2), 35% (S3), 24% (S4), 9% (S5), 6% (S6), 3% (S7), 2% (S8), 1% (S9), 1% (S10). In the first ~50 fs of the simulations, the states S_n ($n \geq 5$) transfer their populations to the lowest excited states.

Populations of states S_3 and S_4 decay, whereas S_2 acts as an intermediate state characterized by an initial increase in population followed by a subsequent population loss but at a slower rate. As a result, a highly efficient buildup of the population of the lower S_1 state is observed as a consequence of a $S_4/S_3 \rightarrow S_2 \rightarrow S_1$ sequential mechanism.

We now focus on the analysis of vibrations during nonadiabatic transitions between the states. For this purpose, ES-INM analysis has been performed on both the S_n and S_{n-1} ($n = 3, 2$) states (i.e., ES-INM(S_n) and ES-INM(S_{n-1}), respectively) at the time of effective $S_n \rightarrow S_{n-1}$ transitions. We define an effective transition, or hop, as an effective $S_n \rightarrow S_{n-1}$ transition if no backhopping occurs during the rest of the trajectory. These ES-INM(S_n) and ES-INM(S_{n-1}) basis sets have been used to project the nonadiabatic coupling vector $\mathbf{d}_{n,(n-1)}$ evaluated at the moment of hop.

The direction of the nonadiabatic coupling vector $\mathbf{d}_{n,(n-1)}$ evaluated at the moment of hop has an important physical meaning. As shown in the pioneering works of Pechukas,[78] a stationary phase evaluation of the path integral representation of the nuclear motion while the electronic quantum state with time-dependent Hamiltonian $H_{el}(t)$ undergoes a transition from state α at time t' to state β at time t'' leads to the semiclassical expression of the force $\mathbf{F}_{\alpha\beta}$ for the most important "classical-like" path given as[79,81]

$$F_{\alpha\beta}(\mathbf{R}(t)) = -\mathrm{Re}\left\{ \frac{\langle \psi(\mathbf{r},\mathbf{R},t)|\partial H_{el}/\partial \mathbf{R}(t)|\bar{\psi}(\mathbf{r},\mathbf{R},t)\rangle}{\langle \psi(\mathbf{r},\mathbf{R},t)|\bar{\psi}(\mathbf{r},\mathbf{R},t)\rangle} \right\} \quad (12)$$

where $\psi(\mathbf{r},\mathbf{R},t)$ and $\bar{\psi}(\mathbf{r},\mathbf{R},t)$ are mixed electronic state wave functions representing the solutions of the time-dependent Schrödinger equation with Hamiltonian $H_{el}(t)$. Here $\psi(\mathbf{r},\mathbf{R},t)$ is the wave function initially in basis state $\phi_\alpha(\mathbf{r};\mathbf{R}(t'))$ at time t' and evolving to time t, and $\bar{\psi}(\mathbf{r},\mathbf{R},t)$ is the corresponding wave function initially in basis state $\phi_\beta(\mathbf{r};\mathbf{R}(t''))$ at time t'' and evolving backward in time to t. Substituting the expressions of $\psi(\mathbf{r},\mathbf{R},t)$ and $\bar{\psi}(\mathbf{r},\mathbf{R},t)$ according to eq 1 and, for the sake of simplicity, considering only the two α and β states, it can be shown that $F_{\alpha\beta}(\mathbf{R}(t))$ can be expressed as

$$F_{\alpha\beta}(\mathbf{R}(t)) = c_\alpha^*(t)\, c_\alpha(t)\, F_\alpha(\mathbf{R}(t)) + c_\beta^*(t)\, c_\beta(t)\, F_\beta(\mathbf{R}(t))$$
$$- (c_\alpha^*(t)\, c_\beta(t) E_\beta - c_\beta^*(t)\, c_\alpha(t) E_\alpha)\mathbf{d}_{\alpha\beta} \quad (13)$$

where the following off-diagonal Hellman−Feynman expression has been used

$$\frac{\partial\langle \phi_\alpha(\mathbf{r};\mathbf{R}(t))|H_{el}|\phi_\beta(\mathbf{r};\mathbf{R}(t))\rangle}{\partial \mathbf{R}(t)} = 0$$
$$= \langle \phi_\alpha(\mathbf{r};\mathbf{R}(t))|\partial H_{el}/\partial \mathbf{R}(t)|\phi_\beta(\mathbf{r};\mathbf{R}(t))\rangle - (E_\beta - E_\alpha)\mathbf{d}_{\alpha\beta} \quad (14)$$

Equation 13 illustrates the different contributions to the nuclear forces. The first two terms are simply the population weighted average forces over the adiabatic α and β states. The first term evolves from unity at t' to zero at t'' and the second term concomitantly evolves from zero to unity. The last term indicates the direction of the nonadiabatic coupling vector $\mathbf{d}_{\alpha\beta}$ and represents the nonadiabatic contribution to the nuclear forces. Nevertheless, eqs 12 and 13 must be solved iteratively due to the inconvenient temporal nonlocality of $F_{\alpha\beta}(\mathbf{R}(t))$; i.e., the force on the trajectory at time t depends on the forward and backward propagated wave functions, which can only be

determined if the full trajectory is known. As was previously demonstrated by Coker and Xiao[80] using time-dependent perturbation theory, the dynamically nonlocal eq 12 of classical nuclear motion in the presence of quantum electronic transitions can be localized in time to give an impulsive force, which acts when trajectories hop between electronic surfaces. The action of this force is in the direction of the nonadiabatic coupling vector $\mathbf{d}_{\alpha\beta}$, justifying the adjustment of nuclear momenta in this direction to conserve energy during hops.[81]

In the present case, we are interested in identifying nuclear vibrations that participate in the nonadiabatic contribution to the nuclear forces during the ultrafast through-bond sequential transfer via $S_4/S_3 \rightarrow S_2 \rightarrow S_1$ mechanism of electronic energy transfer between the PPE units. Therefore, we have projected the nonadiabatic coupling vector $\mathbf{d}_{n,(n-1)}$ on the basis set of both ES-INM(S_n) and ES-INM(S_{n-1}) evaluated at the moment of efficient $S_n \rightarrow S_{n-1}$ hops ($t_{n,(n-1)}^{\mathrm{hop}}$) as

$$\mathbf{d}_{n,(n-1)}(t_{n,(n-1)}^{\mathrm{hop}}) = \sum_{j=1}^{3N-6} a_n^j(t_{n,(n-1)}^{\mathrm{hop}})\, \mathbf{Q}_n^j(t_{n,(n-1)}^{\mathrm{hop}})$$

$$\mathbf{d}_{n,(n-1)}(t_{n,(n-1)}^{\mathrm{hop}}) = \sum_{j=1}^{3N-6} b_{(n-1)}^j(t_{n,(n-1)}^{\mathrm{hop}})\, \mathbf{Q}_{(n-1)}^j(t_{n,(n-1)}^{\mathrm{hop}})$$
$$(15)$$

Figure 3 depicts the histograms of the maximum $a_n^{\max}(t_{n,(n-1)}^{\mathrm{hop}})$ and $b_{(n-1)}^{\max}(t_{n,(n-1)}^{\mathrm{hop}})$ values among the set of coefficients
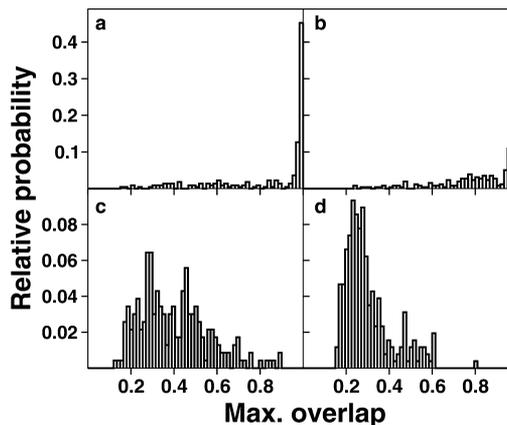
Figure 3. Histograms of the maximum overlaps between the nonadiabatic coupling vector $\mathbf{d}_{3,2}$ and an excited-state instantaneous normal mode (ES-INM) calculated on (a) the S_3 state and (b) the S_2 state, both during effective $S_3 \rightarrow S_2$ hops, and overlaps between $\mathbf{d}_{2,1}$ and an ES-INM calculated on (c) the S_2 state and (d) the S_1 state, during effective $S_2 \rightarrow S_1$ hops.

$\{a_n^j(t_{n,(n-1)}^{\mathrm{hop}})\}_{j=1,3N-6}$ and $\{b_{(n-1)}^j(t_{n,(n-1)}^{\mathrm{hop}})\}_{j=1,3N-6}$ during effective $S_3 \rightarrow S_2$ hops (Figure 3a), and $S_2 \rightarrow S_1$ hops (Figure 3b). As can be seen in Figure 3a,b, $a_n^{\max}(t_{n,(n-1)}^{\mathrm{hop}})$ reaches the overlap values ≈ 1 in both transitions, indicating that the direction of $\mathbf{d}_{n(n-1)}$ perfectly matches with the direction given by only one ES-INM(S_n), i.e.

$$\mathbf{d}_{n(n-1)}(t_{n,(n-1)}^{\mathrm{hop}}) \approx \mathbf{Q}_n^{\max}(t_{n,(n-1)}^{\mathrm{hop}}) \quad (16)$$

Therefore, eq 16 indicates that, at the moment of strong interaction between the excited electronic S_n and $S_{(n-1)}$ states ($n = 3, 2$), the energy between states flows in the direction of one of the instantaneous nuclear vibrations on the "upper" S_n

state. That is, the existence of this $\mathbf{Q}_n^{max}(t_{n,(n-1)}^{hop})$ can be interpreted as a crucial factor for the efficiency of the electronic energy-transfer processes. Interestingly, this mode corresponds to the highest frequency ES-INM(S_n). On the contrary, significantly lower values of $b_{(n-1)}^{max}(t_{n,(n-1)}^{hop})$, shown in Figure 3c,d, indicate that, after the $S_n \rightarrow S_{(n-1)}$ transfer, the energy received by the "lower" $S_{(n-1)}$ state is spread out in the direction of multiple vibrations. This effectively leads to dissipation of vibrational energy and a reduced efficiency of the backward $S_{(n-1)} \rightarrow S_n$ transfers.

According to a sequential $S_{n+1} \rightarrow S_n \rightarrow S_{n-1}$ mechanism,[73] our findings shown in Figure 3 can be summarized as follows. If the S_{n+1} and S_n states are coupled, a state-specific vibration on the S_{n+1} state, given by the $\mathbf{Q}_{(n+1)}^{max}(t_{(n+1),n}^{hop})$ mode, appears to create an efficient $S_{n+1} \rightarrow S_n$ pathway, whereas there are no analogous vibrations on the S_n state. Therefore, nuclear differential motions on the two potential energy surfaces are responsible for the highly efficient $S_{n+1} \rightarrow S_n$ population transfer compared to the corresponding slow backward $S_n \rightarrow S_{n+1}$ transfer. On the other hand, once the system leaves the region of conformational space associated with the high values of $\mathbf{d}_{(n+1),n}$ to reach regions with high $\mathbf{d}_{n,(n-1)}$ values, the state-specific vibration $\mathbf{Q}_n^{max}(t_{n,(n-1)}^{hop})$, now on the S_n state, enhances the $S_n \rightarrow S_{n-1}$ transfer but no S_{n-1} vibrations have been found to match with the backward $S_{n-1} \rightarrow S_n$ direction.

We next analyze the evolution properties of both $\mathbf{Q}_3^{max}(t_{3,2}^{hop})$ and $\mathbf{Q}_2^{max}(t_{2,1}^{hop})$ corresponding to the nonadiabatic coupling vectors $\mathbf{d}_{3,2}(t_{3,2}^{hop})$ and $\mathbf{d}_{2,1}(t_{2,1}^{hop})$, respectively. Figure 4 displays
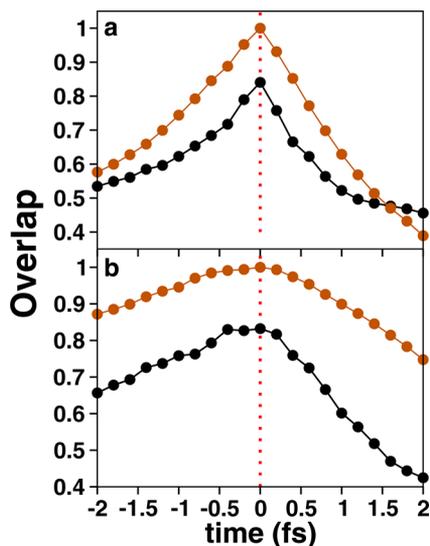
Figure 4. Time dependence of (a) the overlap between the nonadiabatic coupling vectors $\mathbf{d}_{3,2}(t_{3,2}^{hop})$ and $\mathbf{d}_{3,2}(t-t_{3,2}^{hop})$ (brown) and the overlap between $\mathbf{d}_{3,2}(t_{3,2}^{hop})$ and $\mathbf{Q}_3^{max}(t-t_{3,2}^{hop})$ (black). (b) Overlap between nonadiabatic coupling vectors $\mathbf{d}_{2,1}(t_{2,1}^{hop})$ and $\mathbf{d}_{2,1}(t-t_{2,1}^{hop})$ (brown) and the overlap between $\mathbf{d}_{2,1}(t_{2,1}^{hop})$ and $\mathbf{Q}_2^{max}(t-t_{2,1}^{hop})$ (black). Results are averaged over all the trajectories.

the evolution of corresponding overlaps during the $[t_{3,2}^{hop} - 2\,fs: t_{3,2}^{hop} + 2\,fs]$ and $[t_{2,1}^{hop} - 2\,fs: t_{2,1}^{hop} + 2\,fs]$ time intervals. First, the identities of the $\mathbf{d}_{3,2}(t_{3,2}^{hop})$ and $\mathbf{d}_{2,1}(t_{2,1}^{hop})$ vectors were tracked as they change in time by evaluating the overlaps $\mathbf{d}_{3,2}(t_{3,2}^{hop}) \cdot \mathbf{d}_{3,2}(t-t_{3,2}^{hop})$ and $\mathbf{d}_{2,1}(t_{2,1}^{hop}) \cdot \mathbf{d}_{2,1}(t-t_{2,1}^{hop})$, respectively. In both cases, the loss of identity of the $\mathbf{d}_{n,(n-1)}$ ($n = 3, 2$) vector is faster when the nuclei are moving on the S_{n-1} state than on S_n. This behavior is consistent with the idea that the nuclear motions on the

"upper" S_n potential energy surface keep the system in regions of conformational space with high values of $\mathbf{d}_{n,(n-1)}$ (i.e., closer to its average maximum value at $t_{n,(n-1)}^{hop}$) whereas vibrational motions on the "lower" S_{n-1} state do not. In addition, the faster decay of these overlaps for the S_3-S_2 couplings compared to those of S_2-S_1 indicates that changes in the corresponding electronic populations are more localized in the former case than in the latter. Figure 4 also shows the time dependence of the overlaps $\mathbf{d}_{3,2}(t_{3,2}^{hop}) \cdot \mathbf{Q}_3^{max}(t-t_{3,2}^{hop})$ and $\mathbf{d}_{2,1}(t_{2,1}^{hop}) \cdot \mathbf{Q}_2^{max}(t-t_{2,1}^{hop})$. In both cases, the average maximum values are achieved at the moment of the hop. Nevertheless, as the identity of these INMs evolve in time, they may mix with the other coordinates and, therefore, $\mathbf{Q}_n^{max}(t_{n,(n-1)}^{hop})$ ($n = 3, 2$), as defined at the moment of efficient $S_n \rightarrow S_{n-1}$ hops ($t_{n,(n-1)}^{hop}$), exhibit very short lifetimes.[82]

These features are related to ultrafast geometry distortions introduced by the nuclear motion on the "lower" S_{n-1} potential energy surface immediately after the hop. Furthermore, the participation values[83,84] corresponding to the projections of $\mathbf{d}_{3,2}(t_{3,2}^{hop})$ and $\mathbf{d}_{2,1}(t_{2,1}^{hop})$ on the entire basis set of the ES-INM(S_3) and ES-INM(S_2), respectively, i.e.

$$\mathbf{P}_{\mathbf{d}_{n,(n-1)}}^n(t) = \left(\sum_{j=1}^{3N-6} (a_n^j(t))^4 \right)^{-1} \qquad (n = 3, 2)$$

(17) reach values of $\mathbf{P}_{\mathbf{d}_{n,(n-1)}}^n(t) \approx 5$ in only 2 fs after both $S_3 \rightarrow S_2$ and $S_2 \rightarrow S_1$ transitions. That is, the energy, initially funneled through the $\mathbf{Q}_3^{max}(t_{3,2}^{hop})$ and $\mathbf{Q}_2^{max}(t_{2,1}^{hop})$ vectors, is rapidly scattered to at least 5 different modes.

In Figure 5a,b we present $\mathbf{Q}_3^{max}(t_{3,2}^{hop})$ and $\mathbf{Q}_2^{max}(t_{2,1}^{hop})$ for typical trajectories at the time of the effective $S_3 \rightarrow S_2$ and $S_2 \rightarrow$
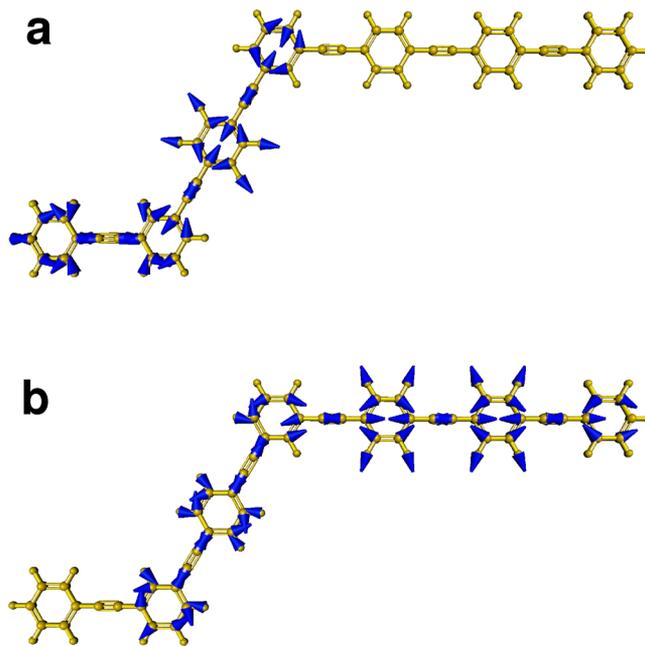
Figure 5. (a) 252th ES-INM(S_3), i.e., $\mathbf{Q}_3^{max}(t_{3,2}^{hop})$. (b) 252th ES-INM($S_2$), i.e, $\mathbf{Q}_2^{max}(t_{2,1}^{hop})$.

S_1 transitions, respectively. Singular value decomposition (SVD) has been performed over both sets of $\mathbf{Q}_3^{max}(t_{3,2}^{hop})$ and $\mathbf{Q}_2^{max}(t_{2,1}^{hop})$ for all the trajectories. The eigenvectors of the first singular values have shown an average overlap of 0.8 ± 0.15 and 0.87 ± 0.16 with the originals $\mathbf{Q}_3^{max}(t_{3,2}^{hop})$ and $\mathbf{Q}_2^{max}(t_{2,1}^{hop})$, respectively, indicating the high similarity between them. The

atomic displacements of the $\mathbf{Q}_3^{max}(t_{3,2}^{hop})$ modes are mostly distributed between the two-ring (~50%) and the three-ring (~40%) linear PPE units. As shown in Figure 5a, these modes represent a concerted motion of stretchings in the direction of the ethynylene bonds and the highest frequency A_{1g} vibrational normal modes of phenyl rings (collective C—H stretch at 3385 cm^{-1} in benzene, ground state). Similarly, as shown in Figure 5b, the atomic displacements of the $\mathbf{Q}_2^{max}(t_{2,1}^{hop})$ modes are mostly distributed between the three-ring (~52%) and the four-ring (~45%) linear PPE units.

As has been pointed out, our analysis of the spatial extent of the state transition densities (S_n–S_0) shows localizations of S_3, S_2, and S_1 states on the two-ring, three-ring, and four-ring units, respectively. Therefore, the existence of the highest frequency modes, $\mathbf{Q}_3^{max}(t_{3,2}^{hop})$ and $\mathbf{Q}_2^{max}(t_{2,1}^{hop})$, with atomic displacements distributed between the two-ring and three-ring, and between the three-ring and four-ring units, respectively, is consistent with their roles as pathways through which the efficient energy funneling takes place.

Both $\mathbf{Q}_3^{max}(t_{3,2}^{hop})$ and $\mathbf{Q}_2^{max}(t_{2,1}^{hop})$ can also be projected on the basis of equilibrium normal modes calculated on the electronic ground state (ENM-S_0), to evaluate the existence of these modes in the ground state. The participation numbers corresponding to these projections are 4.6 and 3.8, respectively. Therefore, neither the $\mathbf{Q}_3^{max}(t_{3,2}^{hop})$ mode nor the $\mathbf{Q}_2^{max}(t_{2,1}^{hop})$ mode has equivalent counterparts in the ground state. These results reinforce the notion that state-specific normal modes are associated with nonadiabatic coupling of excited states during the intramolecular energy-transfer process.

Finally, the intramolecular electronic energy redistribution that accompanies the changes in the vibrational motions can be followed by analyzing the time evolution of the nth-electronic transition density $\rho^{g-n}(t)$ (g and n label ground and nth excited state, respectively) computed according to the CEO procedure.[25,85] Figure 6 shows the time dependence of both

$\rho^{g-3}(t)$ and $\rho^{g-2}(t)$ evaluated as the atomic overlaps with the nonadiabatic coupling vectors $\mathbf{d}_{3,2}(t_{3,2}^{hop})$ and $\mathbf{d}_{2,1}(t_{2,1}^{hop})$ during the $[t_{3,2}^{hop} - 2\ \text{fs}: t_{3,2}^{hop} + 2\ \text{fs}]$ and $[t_{2,1}^{hop} - 2\ \text{fs}: t_{2,1}^{hop} + 2\ \text{fs}]$ time intervals, respectively. As has been shown for $\mathbf{Q}_n^{max}(t_{n,(n-1)}^{hop})$ (n = 3, 2) modes, the average maximum values are achieved at the moment of the hop. Also changes in $\rho^{g-n}(t)$ are faster when the nuclei are moving on the S_{n-1} state than on S_n. That is, the behavior of $\rho^{g-n}(t)$ follows that of the $\mathbf{Q}_n^{max}(t_{n,(n-1)}^{hop})$ (n = 3, 2) modes. Although $\rho^{g-3}(t)$ is delocalized between the two-ring and the three-ring linear PPE units during the $S_3 \rightarrow S_2$ transfers, $\rho^{g-2}(t)$ is delocalized between the three-ring and the four-ring linear PPE units during the $S_2 \rightarrow S_1$ transfers. These features indicate the mixture of the electronic states during the transfers.

IV. CONCLUSIONS

We have combined the nonadiabatic excited-state molecular dynamics (NA-ESMD) approach and excited-state instantaneous normal modes (ES-INM) analysis to describe the state-specific vibrational modes that lead to the highly efficient and unidirectional energy transfer between the individual coupled chromophore units in the branched dendritic molecule. Our model molecular system consists of two-, three-, and four-ring linear poly(phenyleneethynylene) (PPE) units linked through meta-positions.

Our analysis of vibrations during the nonadiabatic transitions $S_n \rightarrow S_{(n-1)}$ (n = 3, 2) shows that the nonadiabatic contribution to the forces, given in the direction of the nonadiabatic coupling vector $\mathbf{d}_{n(n-1)}$, perfectly matches with the direction given by the highest frequency instantaneous vibrational mode on the "upper" S_n state. We show that the direction of the nonadiabatic coupling vector, which can be interpreted as the direction of the driving force propagating the instantaneous molecular configurations throughout regions of strong coupling, actually acts along this unique instantaneous normal mode direction. This provides a simple physical rationale for adjusting nuclear velocities along the direction of the nonadiabatic coupling vector following hops between electronic states prescribed by the MDQT algorithm. This highest frequency INM of the "upper" S_n state does not have a counterpart among the INMs on the "lower" $S_{(n-1)}$ state. Hence, upon the nonadiabatic transition, the excess electronic energy is being dissipated among the multiple INMs of the "lower" $S_{(n-1)}$ state reducing the efficiency of backward $S_{(n-1)} \rightarrow S_n$ transfers. Therefore, our results can be interpreted as a crucial feature of the efficient energy funneling observed in light-harvesting dendrimers.

The analysis of the INMs that participate in the nonadiabatic transitions indicates that their lifetimes are mainly restricted to times close to the electronic transitions. In all cases, these modes represent a concerted motion of stretchings in the direction of the ethynylene bonds along with the participation of high frequency C—H vibrations of phenyl rings. Furthermore, taking into account the localization of the S_3, S_2, and S_1 state transition densities on the two-ring, three-ring, and four-ring units, respectively, the distribution of the atomic displacement involved in each of these modes reveals their roles as "bridges" through which the efficient energy funneling takes place.

According to the sequential $S_{n+1} \rightarrow S_n \rightarrow S_{n-1}$ mechanism, we can conclude that unique state-specific vibrations on the S_{n+1} and S_n states contribute to create the efficient funneling at the intermediate $S_{n+1} \rightarrow S_n$ and $S_n \rightarrow S_{n-1}$ steps, respectively. Therefore, our results suggest studies of the unidirectional

Figure 6. Time dependence of (a) the overlap between the nonadiabatic coupling vectors $\mathbf{d}_{3,2}(t_{3,2}^{hop})$ and the electronic transition density of S_3, $\rho^{g-3}(t-t_{3,2}^{hop})$. (b) Overlap between nonadiabatic coupling vectors $\mathbf{d}_{2,1}(t_{2,1}^{hop})$ and the electronic transition density of S_2, $\rho^{g-2}(t-t_{2,1}^{hop})$. Results are averaged over all the trajectories.

energy transfer using hybrid quantum/classical simulations in which only the state-specific vibrational modes directly involved in the process are treated quantum mechanically.

■ AUTHOR INFORMATION

Corresponding Author
*E-mail: sfalberti@gmail.com.

Notes
The authors declare no competing financial interest.

■ ACKNOWLEDGMENTS

■ REFERENCES

(1) Katz, A. I.; Apkarian, V. A. *J. Phys. Chem.* **1990**, *94*, 6671−6678.

(2) Fraenkel, R.; Y. Haas, Y. *Chem. Phys. Lett.* **1993**, *214*, 234−240.

(3) LaBrake, D.; Ryan, E.; Weitz, E. *J. Chem. Phys.* **1995**, *102*, 4112−4122.

(4) Ashfold, M.; Simons, J. *J. Chem. Soc., Faraday Trans. 2* **1978**, *74*, 280−291.

(5) Fisher, W.; Carrington, T.; Filseth, S.; Sadowski, C.; Dugan, C. *Chem. Phys.* **1983**, *82*, 443−457. Fisher, W.; Eng, R.; Carrington, T.; Dugan, C.; Filseth, S.; Sadowski, C. *Chem. Phys.* **1984**, *89*, 457−471. Dugan, C.; Anthony, D. *J. Phys. Chem.* **1987**, *91*, 3929−3932. Dugan, C. *J. Phys. Chem.* **1988**, *92*, 720−722.

(6) Marinelli, W.; Sivakumar, N.; Houston, P. *J. Phys. Chem.* **1984**, *88*, 6685. Hall, G.; Sivakumar, N.; Houston, P. *J. Chem. Phys.* **1986**, *84*, 2120−2128. Goldfield, E. M.; Houston, P.; Ezra, G. S. *J. Phys. Chem.* **1986**, *84*, 3120−3129.

(7) Shortreed, M. R.; Swallen, S. F.; Shi, Z. Y.; Tan, W. H.; Xu, Z. F.; Devadoss, C.; Moore, J. S.; Kopelman, R. *J. Phys. Chem. B* **1997**, *101*, 6318−6322.

(8) Kopelman, R.; Shortreed, M.; Shi, Z. Y.; Tan, W. H.; Xu, Z. F.; Moore, J. S.; Bar-Haim, A.; Klafter, J. *Phys. Rev. Lett.* **1997**, *78*, 1239−1242.

(9) Mukamel, S. *Nature* **1997**, *388*, 425−427.

(10) Swallen, S. F.; Kopelman, R.; Moore, J. S.; Devadoss, C. *J. Mol. Struct.* **1999**, *485*, 585−597.

(11) Fréchet, J. M. J. *Science* **1994**, *263*, 1710−1715.

(12) Rana, D.; Gangopadhyay, G. *Chem. Phys. Lett.* **2001**, *334*, 314−324.

(13) Swallen, S. F.; Zhu, Z.; Moore, J. S.; Kopelman, R. *J. Phys. Chem. B* **2000**, *104*, 3988−3995.

(14) Devadoss, C.; Bharathi, P.; Moore, J. S. *J. Am. Chem. Soc.* **1996**, *118*, 9635−9644.

(15) Xu, Z.; Kahr, M.; Walker, K. L.; Wilkins, C. L.; Moore, J. S. *J. Am. Chem. Soc.* **1994**, *116*, 4537−4550.

(16) Wu, C; Malinin, S. V.; Tretiak, S.; Chernyak, V. Y. *Nat. Phys.* **2006**, *2*, 631−638.

(17) Palma, J. L.; Atas, E.; Hardison, L.; Marder, T. B.; Collings, J. C.; Beeby, A.; Melinger, J. S.; Krause, J. L.; Kleiman, V. D.; Roitberg, A. E *J. Phys. Chem. C* **2010**, *114*, 20702−20712.

(18) Atas, E.; Peng, Z.; Kleiman, V. D. *J. Phys. Chem. B* **2005**, *109*, 13553−13560.

(19) Kleiman, V. D.; Melinger, J. S.; McMorrow, D. *J. Phys. Chem. B* **2001**, *105*, 5595−5598.

(20) Kuroda, D. G.; Sing, C. P.; Peng, Z.; Kleiman, V. D. *Science* **2009**, *326*, 263−267.

(21) Davydov, A. S. *Theory of Molecular Excitons*; Plenum: New York, 1971.

(22) (a) Rashba E. I., Sturge, M. D., Eds. *Excitons*; North Holland: Amsterdam, 1982. (b) Broude, V. B.; Rashba, E. I.; Sheka, E. F. *Spectroscopy of Molecular Excitons*; Springer: Berlin, 1985.

(23) Poliakov, E. Y.; Chernyak, V.; Tretiak, S.; Mukamel, S. *J. Chem. Phys.* **1999**, *110*, 8161−8175.

(24) Minami, T.; Tretiak, S.; Cherniak, V.; Mukamel, S. *J. Lumin.* **2000**, *87−89*, 115−118.

(25) Tretiak, S.; Chernyak, V.; Mukamel, S. *J. Am. Chem. Soc.* **1997**, *119*, 11408−11419.

(26) Mukamel, S.; Tretiak, S.; Wagersreiter, T.; Chernyak, V. *Science* **1997**, *277*, 781−787.

(27) Nelson, T.; Fernandez-Alberti, S.; Chernyak, V.; Roitberg, A. E.; Tretiak, S. *J. Phys. Chem. B* **2011**, *115*, 5402−5414, in the "Shaul Mukamel Festschrift".

(28) Nishikawa, T.; Go, N. *Struct. Funct. Genet.* **1987**, *2*, 308−329.

(29) Brooks, B. R.; Karplus, M. *Proc. Natl. Acad. Sci. U. S. A* **1983**, *80*, 6571−6575.

(30) McCammon, J. A.; Harvey, S. C. *Dynamics of Proteins and Nucleic Acids*; Cambridge University Press: Cambridge, U.K., 1987.

(31) Brooks, B. R.; Karplus, M.; Pettitt, B. M. *Adv. Chem. Phys.* **1988**, *71*, 1−259.

(32) Buchner, M.; Ladanyi, B.; Stratt, R. M. *J. Chem. Phys.* **1992**, *97*, 8522−8535.

(33) Keyes, T. *J. Phys. Chem. A* **1997**, *101*, 2921−2930.

(34) Stratt, R. M. The molecular mechanism behind the vibrational population relaxation of small molecules in liquids. In *Ultrafast infrared and Raman spectroscopy*; Fayer, M. D., Ed.; Marcel Dekker Inc.: Amsterdam, 2001; pp 149−190.

(35) Moore, P.; Tokmakoff, A.; Keyes, T.; Fayer, M. D. *J. Chem. Phys.* **1995**, *103*, 3325−3334.

(36) Goodyear, G; Stratt, R. M. *J. Chem. Phys.* **1997**, *107*, 3098−3120.

(37) David, E. F.; Stratt, R. M. *J. Chem. Phys.* **1998**, *109*, 1375−1390.

(38) Garberoglio, G.; Vallauri, R. *Physica A* **2002**, *314*, 492−500.

(39) Kramer, N.; Buchner, M.; Dorfmuller, T. *J. Chem. Phys.* **1998**, *109*, 1912−1919.

(40) Moore, P. B.; Ji, X. D.; Ahlborn, H.; Space, B. *Chem. Phys. Lett.* **1998**, *296*, 259−265.

(41) Deng, Y. Q.; Ladanyi, B. M.; Stratt, R. M. *J. Chem. Phys.* **2002**, *117*, 10752−10767.

(42) Nguyen, P. H.; Stock, G. *J. Chem. Phys.* **2003**, *119*, 11350−11358.

(43) Sagnella, D. E.; Straub, J. E. *Biophys. J.* **1999**, *77*, 70−84.

(44) Bu, L; Straub, J. E. *Biophys. J.* **2003**, *85*, 1429−1439.

(45) Schulz, R.; Krishnana, M.; Daidone, I.; Smith, J. C. *Biophys. J.* **2009**, *96*, 476−484.

(46) Cho, M.; Fleming, G. R.; Saito, S.; Ohmine, I.; Stratt, R. M. *J. Chem. Phys.* **1994**, *100*, 6672−6683.

(47) Nguyen, P. H.; Park, S.; Stock, G. *J. Chem. Phys.* **2010**, *132*, 025102−025111.

(48) Park, S.; Nguyen, P. H.; Stock, G. *J. Chem. Phys.* **2009**, *131*, 184503−184513.

(49) Bastida, A.; Soler, M. A.; Zuñiga, J.; Requena, A.; Kalstein, A.; Fernandez-Alberti, S. *J. Phys. Chem. A* **2010**, *114*, 11450−11461.

(50) Bastida, A.; Soler, M. A.; Zuñiga, J.; Requena, A.; Kalstein, A.; Fernandez-Alberti, S. *J. Chem. Phys.* **2010**, *132*, 224501−224514.

(51) Tretiak, S.; Saxena, A.; Martin, R. L.; Bishop, A. R. *Phys. Rev. Lett.* **2002**, *89*, 097402−097406.

(52) Tretiak, S.; Saxena, A.; Martin, R. L.; Bishop, A. R. *Proc. Natl. Acad. Sci. U. S. A.* **2003**, *100*, 2185−2190.

(53) Worth, G. A.; Robb, M. A.; Lasorne, B. *Mol. Phys.* **2008**, *106*, 2077−2091.

(54) Tretiak, S.; Mukamel, S. *Chem. Rev.* **2002**, *102*, 3171−3212.

(55) Chernyak, V.; Schulz, M. F.; Mukamel, S.; Tretiak, S.; Tsiper, E. V. *J. Chem. Phys.* **2000**, *113*, 36−43.

(56) Tretiak, S.; Isborn, C.; Niklasson, A.; Challacombe, M. *J. Chem. Phys.* **2009**, *130*, 054111−054127.

(57) Furche, F.; Ahlrichs, R. *J. Chem. Phys.* **2002**, *117*, 7433−7447.

(58) Tretiak, S.; Chernyak, V. *J. Chem. Phys.* **2003**, *119*, 8809−8823.

(59) Tommasini, M.; Chernyak, V.; Mukamel, S. *Int. J. Quantum Chem.* **2001**, *85*, 225−238.

(60) Chernyak, V.; Mukamel, S. *J. Chem. Phys.* **2000**, *112*, 3572−3579.

(61) Send, R.; Furche, F. *J. Chem. Phys.* **2010**, *132*, 044107−044119.

(62) Tretiak, S.; Chernyak, V.; Mukamel, S. *J. Chem. Phys.* **1996**, *105*, 8914−8928.

(63) Tretiak, S.; Zhang, W. M.; Chernyak, V.; Mukamel, S. *Proc. Natl. Acad. Sci. U. S. A.* **1999**, *96*, 13003−13008.

(64) Dewar, M. J. S.; Zoebisch, E. G.; Healy, E. F.; Stewart, J. J. P. *J. Am. Chem. Soc.* **1985**, *107*, 3902−3909.

(65) Hammes-Schiffer, S.; Tully, J. C. *J. Chem. Phys.* **1994**, *101*, 4657−4667.

(66) Tully, J. C. *J. Chem. Phys.* **1990**, *93*, 1061−1071.

(67) Tully, J. C. Nonadiabatic Molecular Dynamics. *Int. J. Quantum Chem.* **1991**, *40*, 299−309.

(68) Nelson, T.; Fernandez-Alberti, S.; Chernyak, V.; Roitberg, A. E.; Tretiak, S. *J. Chem. Phys.* **2012**, *136*, 054108−054120.

(69) Tully, J. C. In *Classical and Quantum Dynamics in Condensed Phase Simulations*; Berne, B. J., Ciccotti, G.; Coker, D. F., Eds.; World Scientific: Singapore, 1998; p 489.

(70) Tully, J. C. In *Modern Methods for Multidimensional Dynamics Computations in Chemistry*; Thompson, D. L. Ed.; World Scientific: Singapore, 1998; p 34.

(71) Drukker, K. *J. Comput. Phys.* **1999**, *153*, 225−272.

(72) Paterlini, M. G.; Ferguson, D. M. *Chem. Phys.* **1998**, *236*, 243−252.

(73) Fernandez-Alberti, S.; Kleiman, V. D.; Tretiak, S.; Roitberg, A. E. *J. Phys. Chem. Lett.* **2010**, *1*, 2699−2704.

(74) Fernandez-Alberti, S.; Kleiman, Valeria D.; Tretiak, S.; Roitberg, Adrian E. *J. Phys. Chem A* **2009**, *113*, 7535−7542.

(75) Verlet, L. *Phys. Rev.* **1967**, *159*, 98−103.

(76) Hull, T. E.; Enright, W.; Jackson, K. User's guide for DVERK − A subroutine for solving non-stiff ODEs; Technical Report 100, Department of Computer Science, University of Toronto: Canada, 1976.

(77) *IMSL MATH/LIBRARY Special Functions*; Visual Numerics, Inc.: Houston, TX 77042, USA.

(78) Pechukas, P. *Phys. Rev.* **1969**, *181*, 166−174.

(79) Webster, F.; Rossky, P. J.; Friesner, R. A. *Comput. Phys. Commun.* **1991**, *63*, 494−522. Webster, F.; Schnitker, J.; Friedrichs, M. S.; Friesner, R. A.; Rossky, P. J. *Phys. Rev. Lett.* **1991**, *66*, 3172−3175.

(80) Coker, D. F.; Xiao, L. *J. Chem. Phys.* **1995**, *102*, 496−510.

(81) Tully, J. C. *Int. J. Quantum Chem.* **1991**, *25*, 299−309.

(82) Kalstein, A.; Fernandez-Alberti, S.; Bastida, A.; Soler, M. A.; Farag, M. H.; Zuñiga, J.; Requena, A. *Theor. Chem. Acc.* **2011**, *128*, 769−782.

(83) Bell, R. J.; Dean, O.; Hibbins-Butter, P. *J. Phys. C: Solid State Phys.* **1970**, *3*, 2111−2118.

(84) Taraskin, S. N.; Elliott, S. R. *Phys. Rev. B* **1999**, *59*, 8572−8585.

(85) Tretiak, S.; Chernyak, V.; Mukamel, S. *Chem. Phys. Lett.* **1996**, *259*, 55−61.